







Exploring nanofibrous networks with x-ray photon correlation spectroscopy through a digital twin

Tomas Rosén ^{1,2,3,*} HongRui He ³ Ruifu Wang,³ Korneliya Gordeyeva ^{1,2} Ahmad Reza Motezakker ^{4,2}
 Andrei Fluerasu,⁵ L. Daniel Söderberg ^{1,2} and Benjamin S. Hsiao ³

¹Department of Fibre and Polymer Technology, Royal Institute of Technology, 100 44 Stockholm, Sweden

²Wallenberg Wood Science Center, Royal Institute of Technology, 100 44 Stockholm, Sweden

³Department of Chemistry, Stony Brook University, Stony Brook, New York 11794-3400, USA

⁴Department of Mechanics, KTH Royal Institute of Technology, SE-100 44 Stockholm, Sweden

⁵National Synchrotron Light Source II, Brookhaven National Lab, Upton, New York 11793, USA



(Received 5 December 2022; accepted 27 June 2023; published 27 July 2023)

We demonstrate a framework of interpreting data from x-ray photon correlation spectroscopy experiments with the aid of numerical simulations to describe nanoscale dynamics in soft matter. This is exemplified with the transport of passive tracer gold nanoparticles in networks of charge-stabilized cellulose nanofibers. The main structure of dynamic modes in reciprocal space could be replicated with a simulated system of confined Brownian motion, a digital twin, allowing for a direct measurement of important effective material properties describing the local environment of the tracers.

DOI: [10.1103/PhysRevE.108.014607](https://doi.org/10.1103/PhysRevE.108.014607)

I. INTRODUCTION

The elusive details of the diffusive dynamics in soft matter systems are of interest for many applications, ranging from molecular transport in cells to nanoparticle assembly processes. X-ray photon correlation spectroscopy (XPCS) is gaining interest since it represents a method that has the potential to provide significant contributions. XPCS is made possible by the last generation of synchrotrons and free-electron lasers, and is the x-ray equivalent to dynamic light scattering (DLS) but with the ability to probe visibly opaque systems with negligible effects from multiple scattering [1,2]. The technique also allows studies of direction-dependent dynamics and anomalous diffusion of nanoparticles in complex environments [3,4].

In XPCS, the diffusion and transport dynamics is extracted from a time-resolved sequence of images of speckle patterns representing the reciprocal space on an area detector using the second-order autocorrelation $g_2(q, \tau)$ (τ and q being the delay time and scattering vector, respectively), which is related to the first-order autocorrelation through the Siegert relation $g_1(\tau) = \sqrt{(g_2 - 1)/\beta}$, where β is the instrument dependent speckle contrast [5].

For Brownian motion of equally sized spherical nanoparticles with radius R in a viscous fluid (viscosity η), characterized by linearly time-dependent mean-square displacement (MSD), $g_1(\tau)$ is exponentially decaying with a relaxation rate

of $\Gamma = Dq^n$ with $n = 2$ and $D = k_B T / (6\pi\eta R)$ being the diffusion coefficient. A polydisperse system with a size-dependent distribution of scattering power $A(R, q)$ would give rise to a first-order autocorrelation according to:

$$g_1(q, \tau) = \int_0^\infty A(R, q) e^{-\frac{k_B T}{6\pi\eta R} q^2 \tau} dR. \quad (1)$$

An apparent polydispersity of dynamics could also be the result of particle transport in a heterogeneous environment, with some particles being more or less hindered by the surrounding matrix. This would often be accompanied with a dynamic scaling exponent n showing either subdiffusive ($n > 2$) or superdiffusive ($n < 2$) behavior [6]. Similar anomalous dynamics can be found also in colloidal gels [4].

Other physical phenomena such as glass-forming liquids [5], the decay of g_1 could instead be described by a stretched exponential function $g_1(\tau) = \exp(-[\Gamma\tau]^\gamma)$, with stretching exponent γ . Practically, it can be very difficult to distinguish a stretched exponential with $\gamma < 1$ from the polydisperse case in Eq. (1), owing to either limited temporal resolution of the detector at low τ or less statistics at larger τ . Furthermore, it was argued that assuming a stretched exponential can often conceal dynamic heterogeneity in the data, which would be unveiled using inverse transformation of g_2 through the CONTIN algorithm [7].

The interpretation of experimental data presents a general challenge for scattering methods, which often is addressed through model-based parametric curve fitting after reduction of the data to one-dimensional functions. The correct functional form of the data relies on a correct assumption about the physics in the system or practically noise-free data. The most common approach is to assume a simple or stretched exponential decay of $g_1(\tau)$ with $n = 2$ to obtain a diffusion coefficient that is analyzed. The conclusions drawn from changes to D will mainly depend on comparisons

*trosen@kth.se

Published by the American Physical Society under the terms of the [Creative Commons Attribution 4.0 International](https://creativecommons.org/licenses/by/4.0/) license. Further distribution of this work must maintain attribution to the author(s) and the published article's title, journal citation, and DOI. Funded by [Bibsam](https://www.bibsam.se/).

with theoretical arguments or with experiments of similar systems; both which might have limited applicability owing to idealized assumptions.

In this work, we propose the usage of a numerical simulation that can be directly compared with the experimental results. By matching the shapes of the simulated and experimental $g_2(q, \tau)$, we can reveal the details of the dynamics. The simulation operates as a digital twin of the experiment that can (i) reproduce experimental observables, and (ii) provide a direct link between the reduced data provided by the experiment and the mechanisms.

II. EXPERIMENTAL SYSTEM

The model system applied here consists of 200 nm gold nanoparticles (GNPs) distributed in low concentration networks formed by a cellulose nanofibers (CNFs). This does not only present a model of general nanofiber-nanoparticle interactions, but the ability to control and optimize the dynamics of CNF dispersions plays an imperative role in the development of processes [8,9] for new advanced biobased materials [10–12]. Examples of these material concepts are strong filaments for biobased composites [10,13–15], membranes for water purification [16,17], aerogels for therapeutic delivery [18], or artificial tissues and wound dressings in the biomedical field [19,20]. At very low concentrations, CNF dispersions provide a structural scaffold for nanoparticles, allowing hybrid materials that are conductive, magnetic, fire retardant, or provide structural coloring and biosensing abilities [21–28].

To promote generality, two types of CNFs are used. Although these are based on the same raw material (paper pulp) and produced using the same protocol [29], they are produced with different degrees of oxidation, high (HO) and low (LO). The two main effects of the degree of oxidation are (i) different amounts of charged carboxylate (COO^-) groups on the CNF surfaces, resulting in different electrostatic repulsion, and (ii) higher oxidation leads to shorter and thinner nanofibers. The latter also gives a more homogenous spatial mass distribution, as well as smaller network pore (mesh) sizes ξ at a given concentration [see Fig. 1(a)]. This is supported by the characterization of the CNF dispersions [29].

Given these considerations, the transport properties of GNPs in LO CNF and HO CNF will differ at a given concentration. Additionally, assuming a system of randomly oriented rods [29,30], we estimate mesh sizes in the range of $\xi \in [80, 140]$ nm depending on concentration, which implies that the 200 nm GNPs are likely in contact with nanofibers at all times. However, it is worth noting that the network structures even at semidilute conditions are highly dynamic and undergoing constant reorganizations on timescales that are shorter than the timescales for the thermal motion of the GNPs. To provide an experimental system where all relevant time scales can be captured with XPCS, the CNF-GNP system is dispersed in propylene glycol [31].

III. XPCS EXPERIMENTS

The GNP transport dynamics is studied at six states of nanofiber network topology, spanning from dilute state with a few contact points per nanofiber to a semidilute state typically

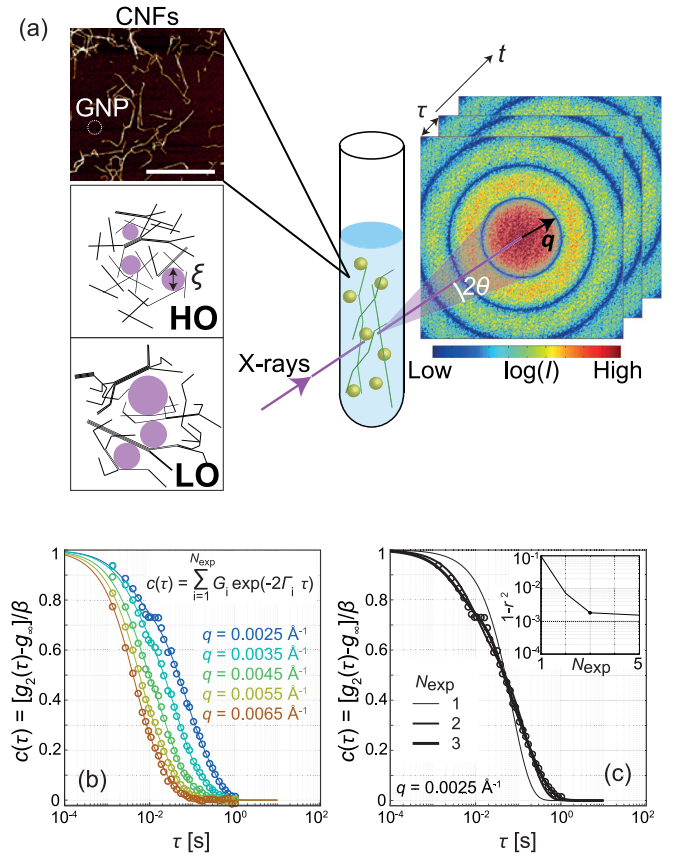


FIG. 1. Experiment and characterization; (a) XPCS experiment of 200 nm sterically stabilized GNPs in CNF; top inset shows an AFM image CNFs (scale bar 1 μm); dashed circle indicates GNP size; the bottom insets indicate the difference between HO CNF and LO CNF, (pore sizes ξ indicated in purple); (b) representative $c(\tau) = (g_2(\tau) - g_\infty)/\beta$ at various q (HO CNF at 0.24 wt%); the solid curves show the fitting results; (c) illustration of the fitting procedure using a sum of N_{exp} exponential modes; the inset figure shows the quality of the fit $1 - r^2$ (with coefficient of determination r^2) for various N_{exp} .

used for material processes [14]. Specifically, three concentrations: 0.08, 0.16, and 0.24 wt%, are used for each of the two levels of oxidation. CNF-GNP samples were mixed and studied using XPCS at the CHX beamline (11-ID) at NSLS-II, Brookhaven National Laboratory, USA (see Fig. 1) [29]. In brief, a coherent x-ray beam (wavelength λ) is focused on the sample and the time-dependent scattering intensity $I(q)$ is recorded on an area detector at various $q = (4\pi/\lambda) \sin \theta$ (with scattering angle 2θ). The scattering intensity is dominated by the GNPs.

By recording a sequence of speckle patterns with delay time τ , the average second-order autocorrelation of the speckle intensities over time $g_2(\tau)$ at a certain q can be quantified, and the scaled and baseline-corrected g_2 is obtained by $c(\tau) = (g_2 - g_\infty)/\beta$, where g_∞ is the baseline [assuming $g_\infty = g_2(q, \tau > 5 \text{ s})$] and β is the speckle contrast found through initial calibration with a test membrane). The Brownian motion in the sample can then be quantified using the decay of $c(\tau)$.

Radiation damage to the CNFs and GNPs was assessed, and it was found that effects could be observed for a dose

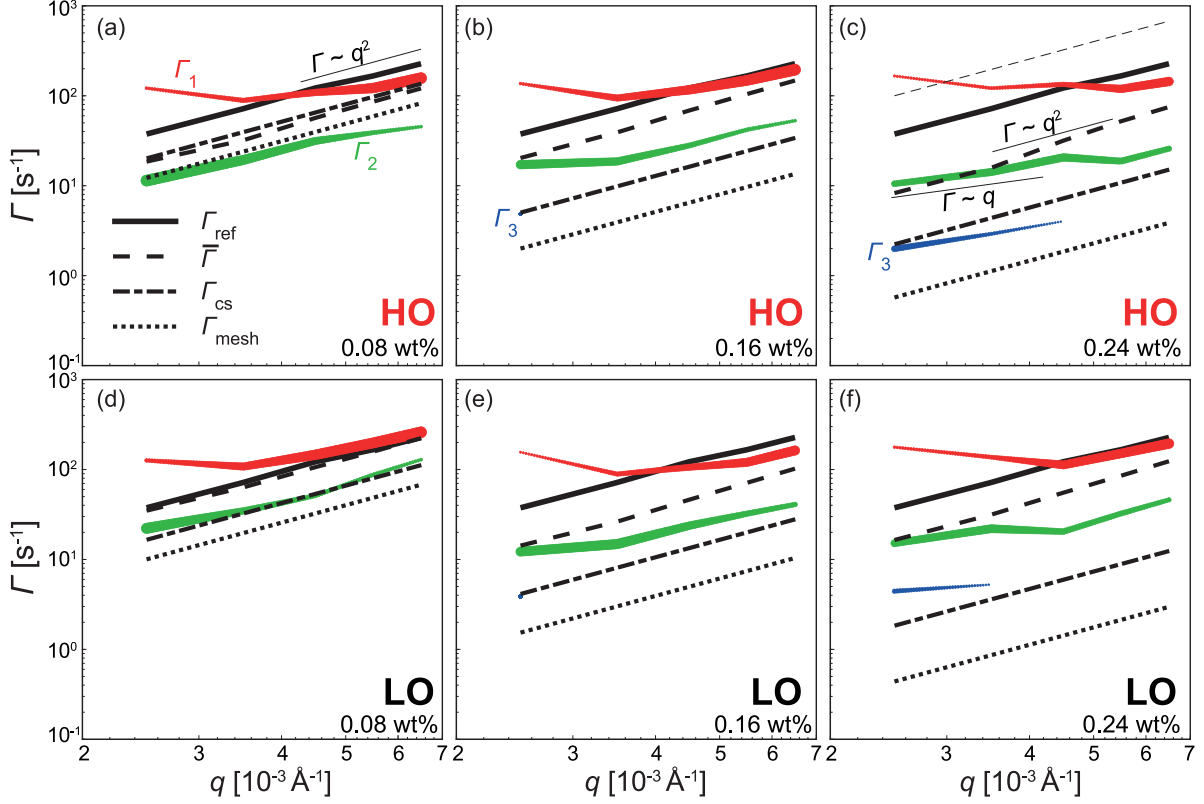


FIG. 2. Relaxation rates of Γ_{1-3} as function of q ; line width gives the magnitude of the modes G_{1-3} , with linear interpolation between the q values ($\sum_i G_i = 1$ at any given q); the thick black solid, dashed, dotted, and dash-dotted lines show the free diffusion of GNPs (Γ_{ref}), mean relaxation rate ($\bar{\Gamma}$), as well as references for mesh regime (Γ_{mesh}) and constraint release (Γ_{cs}), respectively; (a)–(c) dynamic behavior in HO CNF (0.08, 0.16, and 0.24 wt%), while (d)–(e) show the behavior in LO CNF at the same concentrations.

equivalent to >5 s of exposure from the nonattenuated beam [29]. Furthermore, each sample was studied at two attenuation levels, 0% (full beam) and 81% beam attenuation. No significant attenuation-dependent trends were found in the data and since very similar dynamics in reciprocal space was reproduced with the digital twin, regardless of dose [29], it is unlikely that the radiation dose used has any effect on the dynamics. Additionally, repeated measurements were performed at different spatial positions, and thermal equilibrium was ensured [29]. Effects of gravity-induced sedimentation were examined and determined to be negligible [29].

A. Parameterization of autocorrelation data

To describe the shape of the $c(\tau)$ curve at a certain q , the data is parameterized through a fitting procedure, where the functional form provides an accurate shape of the curve without overfitting, but does not need to be based on physics. We emphasize here that any functional form is allowed for the fitting as long as it fulfills these requirements.

Here, $c(\tau)$ is assumed as a sum of exponential modes:

$$c(\tau) = \sum_{i=1}^{N_{\text{exp}}} G_i \exp(-2\Gamma_i \tau), \quad (2)$$

where for each curve, two principles are used to avoid overfitting: (i) either choose the minimum N_{exp} where $1 - r^2 < 10^{-3}$ or (ii) choose the minimum N_{exp} where $r_{N_{\text{exp}}+1}^2 - r_{N_{\text{exp}}}^2 < 10^{-3}$.

Here, r^2 is the ordinary coefficient of determination for the fit [32] and the number of modes never exceeded $N_{\text{exp}} = 3$. The fitting procedure is illustrated in Figs. 1(b), 1(c). The mean decay rate $\bar{\Gamma}$ is found through

$$\ln \bar{\Gamma} = \sum_{i=1}^{N_{\text{exp}}} G_i \ln \Gamma_i. \quad (3)$$

To follow the evolution of the parameterized data as a function of q , the relaxation rates $\Gamma_{1-3}(q)$ are plotted in Fig. 2 with the line widths being scaled with the magnitude of each mode G_{1-3} , respectively. Furthermore, the mean relaxation rate $\bar{\Gamma}(q)$ and the reference of freely diffusing GNPs $\Gamma_{\text{ref}}(q)$, i.e., a system without CNFs [29], are also plotted as thick black dashed and solid lines, respectively. For reference we also plot the expected results assuming some well-known theoretical results. First, at the limit when the mesh size is much smaller than the GNPs (mesh regime) the GNP motion should follow the macroscopic viscosity of the dispersion [33]. Using the CNF zero-shear viscosity η_{CNF} [29], we can calculate the dynamics of this assumption using $\Gamma_{\text{mesh}} = [k_B T / (6\pi \eta_{\text{CNF}} R)] q^2$, which is illustrated in Fig. 2 with the thick dotted line. Second, the dash-dotted line shows the expected results based on the theory by Pryamitsyn and Ganesan [33,34], where the GNP diffusion would be governed by a constraint release motion of the CNFs. Here, $\Gamma_{\text{cs}} = q^2 D_{\parallel} / [\alpha^2 (\alpha + 1)^4 (c_n L^3)^2]$, where $\alpha = R/L$ and $D_{\parallel} = [k_B T / (2\pi \eta L)] [\log r_p - 0.207 + (0.980/r_p) - (0.133/r_p^2)]$

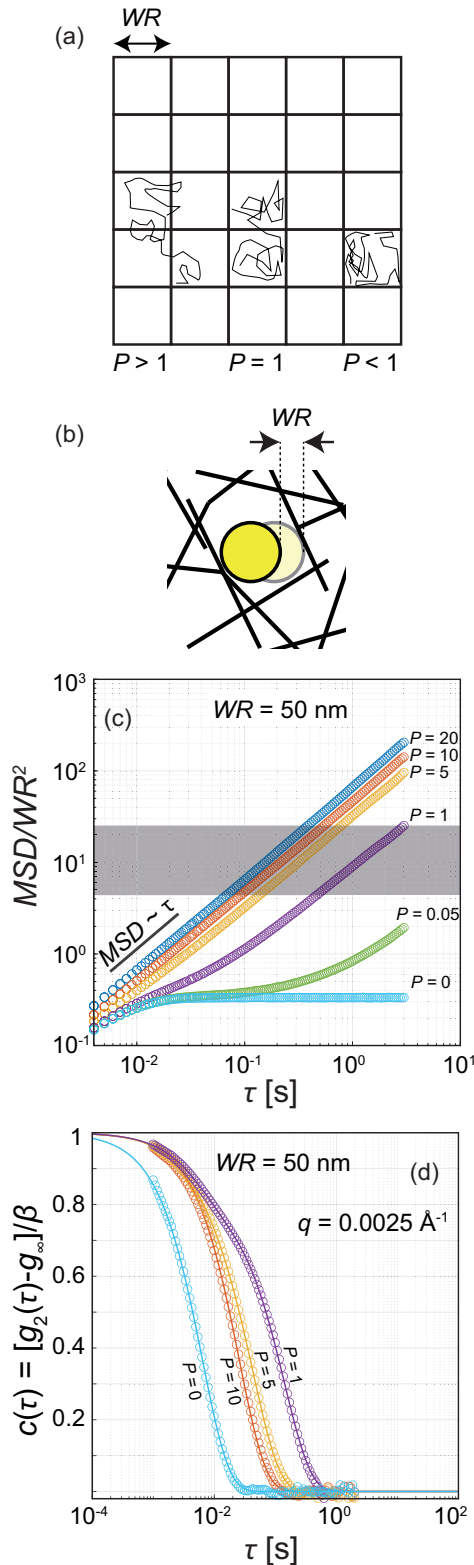


FIG. 3. Digital twin simulation of 200 nm spherical NPs in propylene glycol; (a) simulation domain is divided into cells, where the size determines the wiggles (WR) of the middle position of the NP within which it can move freely; the probability for an NP to cross to another cell is determined by the permeability P ; (b) in the experimental setting, the wiggles WR is the distance a GNP can move without being affected by the surrounding CNFs; (c) mean-squared displacement (MSD) as function of delay time τ of NPs with

according to Tirado *et al.* [35]. The mean CNF length L , aspect ratio r_p and number density c_n are calculated based on the characterization of the CNF dispersions [29].

Several trends can be observed in the figure. At some low threshold concentration (lower than the concentrations considered in this work), there is a transition from single-mode dynamics similar to the free diffusion, to two-mode dynamics: one faster mode Γ_1 that is dominating at high q with relaxation rate almost constant with q ($n \approx 0$), and one slower mode Γ_2 that dominates at lower q and scales as $\Gamma \propto q^2$, albeit with lower relaxation rates compared to the reference.

At higher concentrations, the faster mode Γ_1 remains at the same level as for the lower concentrations, while the slower mode Γ_2 decreases. In the concentration range 0.16 and 0.24 wt%, it transitions towards a scaling of $\Gamma \propto q$ ($n \approx 1$). An even slower mode also appears at low q (denoted Γ_3). Interestingly, even though the contributing modes all seem to be associated with scalings where $n < 2$, the mean rate $\bar{\Gamma}$ appears slightly subdiffusive, i.e., $n > 2$. However, the individual exponential modes are merely used for parametrization of the data to compare shapes of $c(\tau)$ and any physical meaning of these modes will be discussed later. Another interesting observation is the fact that the GNP dynamics, as described by the mean relaxation rate $\bar{\Gamma}$ is much higher than the theoretical models, especially at larger concentrations. The GNPs are thus moving significantly faster than expected based on dispersion viscosity or CNF dimensions.

IV. DIGITAL TWIN OF XPCS EXPERIMENTS

Subdiffusive motion of NPs as an effect of confinement in various semiflexible networks has been demonstrated previously through numerical simulations [6,36,37]. To analyze the dynamics using XPCS, we perform numerical simulations of confined Brownian spherical nanoparticles (NPs) of 200 nm, where their individual positions are used to produce simulated speckle patterns through a Fourier transform, recreating the experimental reciprocal space as observed by the detector.

The model for the digital twin is a two-dimensional (2D) version of the method presented by Ernst *et al.* [36], where NPs are moving within a square grid providing equally sized cells [see Fig. 3(a)], i.e., that the 200 nm NP can move in an undisturbed wiggles room (WR) given by the size of the cell. In the physical system, this wiggles room is given by the distance a GNP can move without its motion being significantly affected by the surrounding CNFs [Fig. 3(b)]. When a time step of the simulated Brownian motion causes the midpoint of the NP to cross the cell boundary, there is a probability of passing determined by a permeability P (unit $s^{-1/2}$). If the NP is not allowed to pass, it simply bounces back and remains in the cell. Thus, $P \rightarrow \infty$, means free diffusion, but if $P \rightarrow 0$, the NP is contained within the cell where it started. In Fig. 3(c), the mean-squared displacement (MSD) of the

←
WR = 50 nm at various P ; the shaded region correspond to the length scales covered with the experimental q range; (d) simulated $c(\tau)$ (circles) from the digital twin with corresponding fits (solid lines).

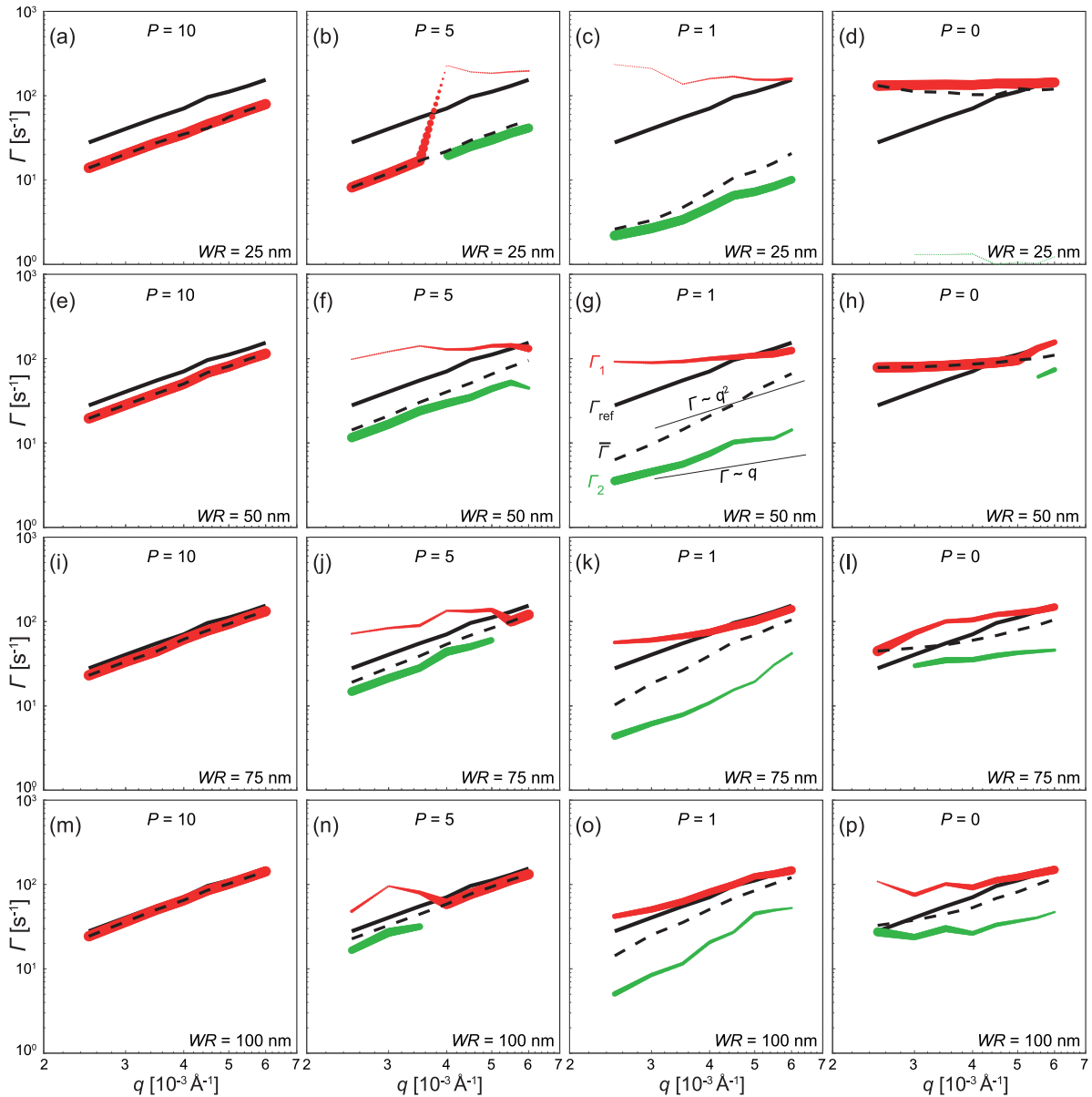


FIG. 4. The evolution of the relaxation rates Γ_{1-3} with respect of q with different permeabilities P illustrated in the same way as in Fig. 2; (a)–(d) $WR = 25$ nm; (e)–(h) $WR = 50$ nm; (i)–(l) $WR = 75$ nm; (m)–(p) $WR = 100$ nm.

NP motion is plotted versus delay time τ at $WR = 50$ nm at various P . At intermediate values of $P \approx 1$, the motion can be seen to be subdiffusive at intermediate τ ($\text{MSD} \propto \tau^{2/n}$, with $n > 2$) when the particle jumps from one cell to another [36,37].

The simulated speckle patterns are analyzed in the same way as the experimental data to obtain the square first-order autocorrelation $c(\tau) = (g_2 - g_\infty)/\beta$ [see Fig. 3(d)], where β is found through exponential extrapolation to $\tau = 0$. The data is then fitted using a sum of exponential modes in the same way as the experimental data. More details of the digital twin model is provided as Supplemental Material [29].

Using the same way to illustrate the fitting results, the simulated relaxation rates Γ_{1-3} are plotted in Fig. 4 with line widths scaled with the magnitudes G_{1-3} . The simulation gives rise to trends which are almost identical to what can be seen in the experimental data, especially for $WR = 50$ and

75 nm. At $P = 10$, the autocorrelation data is described by one single dynamic mode, and with high WR the motion is identical to free diffusion where $\Gamma = Dq^2$. At lower P the dynamic behavior is described with two separate modes, where the faster mode (Γ_1) remains independent of q and higher contribution at higher q . The slower mode (Γ_2) slows down with lower P , and with a diminishing contribution at higher q . Furthermore, looking, e.g., at $WR = 50$ nm and $P = 1$, the contributing modes seem to be associated with scalings where $n < 2$, while the mean rate $\bar{\Gamma}$ appears subdiffusive, just like the experimental data.

At $WR = 25$ and 50 nm, as the contribution of the slower mode diminishes at lower P , the dynamic behavior at $P = 0$ is dominated by the fast stationary mode Γ_1 . Thus, it seems that this mode is linked to the intercell dynamics in the model, while the slower mode could thus be related to the jumping dynamics between cells. However, the autocorrelation is

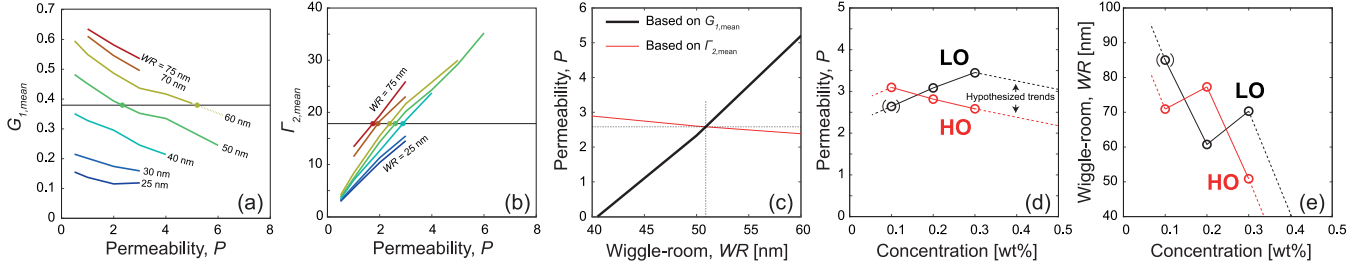


FIG. 5. Quantification of experimental data using the digital twin; (a) mean magnitude of the faster mode $G_{1,\text{mean}}$ and (b) mean relaxation rate of the slower mode $\Gamma_{2,\text{mean}}$ as function of P for various WR ; value of experiment (HO CNF at 0.24 wt%) indicated with solid line; (c) estimation of WR and P using either $G_{1,\text{mean}}$ or $\Gamma_{2,\text{mean}}$; the crossing indicates the only values of WR and P that satisfies both estimations; (d) and (e) shows the values of P and WR for the experimental systems; the data point of LO CNF at 0.08 wt% is put in parenthesis as the value can only be obtained through extrapolation of digital twin data in (a) and (b).

described by a multimodal decay also with zero permeability $WR = 75$ nm or higher, suggesting that it not trivial to attribute the certain modes to certain NP dynamics. The modes should thus only be considered as a means to describe the shape of $c(\tau)$. It should also be noted that the apparent speedup and return to single mode dynamics as $P \rightarrow 0$ is merely an effect of the slowest modes being too slow to be captured without allowing much longer τ , which would be true also for the experimental acquisition.

V. USING THE DIGITAL TWIN FOR QUANTIFICATION

The qualitative similarities of $c(\tau)$ between simulations and experiment suggests that the motion of the GNPs in the CNF networks indeed can be described by the type of confined Brownian motion defined by the digital twin. For a certain range of P and WR , the simulated $c(\tau)$ can be described with a similar bimodal decay in the entire q range as seen in the experiments. We note that no values of P and WR provide a similar trimodal decay as seen at high CNF concentration and low q ; a fact that will be neglected for now, but will be discussed later.

To use the digital twin for quantification, we need to firstly define the range of P and WR with a bimodal decay in the entire q range and thus compare with the experimental data. Secondly, we need establish trends of the modes that are dependent on P and WR . One quantity dependent on both WR and P is the mean magnitude of the first mode $G_{1,\text{mean}}$, which is illustrated in Fig. 5(a), and is seen to decrease with lower WR and higher P . Another quantity is the mean relaxation rate $\Gamma_{2,\text{mean}}$ illustrated in Fig. 5(b), which increases both with WR and P . Using these trends, we can find values of WR and P that satisfies the experimentally obtained $\Gamma_{2,\text{mean}}$ and $G_{1,\text{mean}}$ as illustrated in Fig. 5(c).

This procedure is done for all the experimental cases, where we arrive at quantitative values for WR and P as illustrated in Figs. 5(d) and 5(e). However, the values for LO CNF at 0.08 wt% are put in parenthesis as the value of $\Gamma_{2,\text{mean}}$ was significantly higher than the range in Fig. 5(b) and a value could only be obtained through extrapolation of all the curves in the figure. Other features of the data can of course be used to connect the digital twin to the experiment, but it seems that the assumed confined Brownian motion is not capturing the dynamics well at lower CNF concentrations.

VI. DISCUSSION

The results in this work indicate that the GNPs in the CNF networks follow similar dynamics as the digital twin as the parameterized autocorrelation data have similar trends in the reciprocal space. For engineering purposes, the reduced digital twin model can thus be a helpful tool in describing nanoparticle transport in the nanofiber networks. However, the GNP dynamics ultimately is dependent on the morphology, dynamics and interactions of the surrounding CNFs. We thus need to understand how the model quantities of permeability P and wiggle room WR are related to the physical properties of the CNFs.

As mentioned previously, the typical mesh sizes in the instantaneous random network are significantly smaller than the GNPs, meaning that the immediate surrounding of the individual nanoparticle cannot have the same structure of CNFs as the rest of the network to accommodate the presence of the particle. The surrounding CNFs will likely form a local cage, hindering the CNF motion through the network. At the same time, the semidilute network is dynamic and undergoing constant thermal reconfiguration at time scales depending on concentration. The reconfiguration time scales of CNFs must thus be related to the GNP's ability to escape the local caging structure of CNFs around it, i.e., the permeability P in the digital twin. Similarly, the wiggle room WR must be related to how tightly the CNFs are located around the GNP and the stiffness of the network.

With this physical interpretation of P and WR , it is natural to assume that both quantities should approach zero as the concentration increases and CNFs enter a volume-spanning arrested (gel) state, where GNPs will be completely trapped in the static CNF network. However, the results show that neither P nor WR are monotonically decreasing functions of concentration. Although the permeability in the HO CNF network is following the expected trend [see Fig. 5(d)], the LO CNF shows the opposite trend in the studied concentration regime. We hypothesize that such a trend is possible during the formation of the CNF network, where the Brownian dynamics of CNFs become restricted, thus decreasing the CNF-GNP interactions despite the smaller instantaneous pore sizes at higher concentration. Similar reasoning could also be applied to the wiggle-room, where less dynamic CNFs could give rise to an apparent increase of the space where the GNP

moves freely without interactions. We further hypothesize that the mass heterogeneity of the LO CNF dispersion results in network formation at a comparatively higher volume fraction, which is why the HO CNF already shows a decreasing trend of P and WR at the highest concentration in the study, and that the LO CNF will likely follow this behavior at higher concentrations. It would also make sense that the values of WR and P are higher for the LO CNF when a percolated network is formed owing to the larger physical pore sizes.

Although the reduced model reveals most of the dynamics in the experiment, there are some features missing. For example, the third dynamic mode (Γ_3) with dynamics on larger length scales (lower q). Since the reduced model represents a static cell structure, it is intuitive to assume the presence of modes that are coupled to the CNF network dynamics, a suggestion for future studies. The obvious mismatch with the theoretical models shown in Fig. 2 is rather expected. The mesh regime is likely not reached as it implies that CNFs have negligible dynamics compared to the GNPs. The dynamics for the constraint release mechanism is derived for stiff rods and likely not applicable for the semiflexible CNFs. Furthermore, the subdiffusive motion of GNPs in the CNF network implies that the unit of the diffusion coefficient D would depend on the scaling exponent n and would consequently not be comparable to any theories assuming dynamics where $MSD \propto \tau$. An interesting topic for future studies would thus be to derive new relationships for subdiffusive tracer dynamics that can be applicable for the high-aspect ratio and semiflexible CNFs.

As an outlook, there are several intriguing aspects of using the digital twin approach to XPCS experiments. The digital twin in this work was rather simple to demonstrate the methodology, and a system with isotropic, time-independent dynamics. However, the same approach could be used with a digital twin based on more detailed molecular dynamics simulations with direct control over the physics. The comparison between real and simulated scattering images does not need to be reduced to one-dimensional $g_2(q, \tau)$, but could include comparisons of any anisotropic and time-dependent speckle dynamics. Such dynamics would be expected, for example, with external forcing (e.g., gravity, electrical and magnetic fields, flow deformations, temperature gradients, etc.), which could also be implemented in the digital twin. With the recent advances in artificial intelligence and machine learning, we find that the digital twin approach to the data could become even more advanced. For example, by using the digital twin to create training data for neural networks, sequences of raw scattering images could likely be used to interpret physical phenomena without any data reduction.

VII. CONCLUSIONS

In this work, we have studied the dynamics of gold nanoparticles (GNPs) in networks of cellulose nanofibers (CNFs) using XPCS. Instead of having to assume functional forms of the autocorrelation $g_2(\tau)$ based on theoretical models, we here use a numerical simulation, a digital twin to generate $g_2(\tau)$ curves, which are compared in reciprocal space.

We find that a relatively simple reduced model describing confined Brownian motion can capture the main experimental observations. This in turn allowed us to quantitatively describe the motion of GNPs using the model permeability P and wiggle room WR .

Our work provides a general methodology for exploring nanofibrous systems using tracer NPs and XPCS. Furthermore, the digital twin approach can be enhanced using coarse-grained molecular dynamics simulations. This would not only add more detailed nanofiber properties and interactions, but also reveal phenomena that cannot be measured experimentally. It could also provide training data for machine learning algorithms, allowing physical properties to be directly extracted from experimental data.

As a conclusion, we would like to emphasize that the methodology is not limited to our experimental system but can be used more generally to other nanofibrous networks, e.g., from polymeric, ceramic, or carbon nanotubes.

ACKNOWLEDGMENTS

The authors acknowledge the financial support from the National Science Foundation (DMR-2216585), Wallenberg Wood Science Center (WWSC), the Alf de Ruvo Memorial Foundation and the Hans Werthen Foundation. The authors also acknowledge experimental assistance by C. Zhan, J. Tian, S. Chodankar, and Y. Zhang as well as helpful discussions with F. Lundell, J. Sellberg, M. Nordenström and L. Wågberg. The experiments were performed at the CHX beamline (11-ID) and the LIX beamline (16-ID) of the National Synchrotron Light Source II, a U.S. Department of Energy (DOE) Office of Science User Facility operated for the DOE Office of Science by Brookhaven National Laboratory under Contract No. DE-SC0012704. The Center for BioMolecular Structure (CBMS) is primarily supported by the National Institutes of Health, National Institute of General Medical Sciences (NIGMS) through a Center Core P30 Grant (P30GM133893), and by the DOE Office of Biological and Environmental Research (KP1607011).

-
- [1] A. Nogales and A. Fluerasu, X ray photon correlation spectroscopy for the study of polymer dynamics, *Eur. Poly. J.* **81**, 494 (2016).
- [2] A. R. Sandy, Q. Zhang, and L. B. Lurio, Hard x-ray photon correlation spectroscopy methods for materials studies, *Annu. Rev. Mater. Res.* **48**, 167 (2018).
- [3] A. Pal, M. A. Kamal, T. Zinn, J. K. G. Dhont, and P. Schurtenberger, Anisotropic dynamics of magnetic colloidal

- cubes studied by x-ray photon correlation spectroscopy, *Phys. Rev. Mater.* **5**, 035603 (2021).
- [4] A. Fluerasu, A. Moussaïd, A. Madsen, and A. Schofield, Slow dynamics and aging in colloidal gels studied by x-ray photon correlation spectroscopy, *Phys. Rev. E* **76**, 010401(R) (2007).
- [5] A. Madsen, R. L. Leheny, H. Guo, M. Sprung, and O. Czakkel, Beyond simple exponential correlation functions and

- equilibrium dynamics in x-ray photon correlation spectroscopy, *New J. Phys.* **12**, 055001 (2010).
- [6] R. Metzler, J.-H. Jeon, A. G. Cherstvy, and E. Barkai, Anomalous diffusion models and their properties: Non-stationarity, non-ergodicity, and ageing at the centenary of single particle tracking, *Phys. Chem. Chem. Phys.* **16**, 24128 (2014).
- [7] R. N. Andrews, S. Narayanan, F. Zhang, I. Kuzmenko, and J. Ilavsky, Inverse transformation: Unleashing spatially heterogeneous dynamics with an alternative approach to xpcs data analysis, *J. Appl. Cryst.* **51**, 35 (2018).
- [8] T. Rosén, H. He, R. Wang, C. Zhan, S. Chodankar, A. Fall, C. Aulin, P. T. Larsson, T. Lindström, and B. S. Hsiao, Cross-sections of nanocellulose from wood analyzed by quantized polydispersity of elementary microfibrils, *ACS Nano* **14**, 16743 (2020).
- [9] L. Geng, N. Mittal, C. Zhan, F. Ansari, P. R. Sharma, X. Peng, B. S. Hsiao, and L. D. Söderberg, Understanding the mechanistic behavior of highly charged cellulose nanofibers in aqueous systems, *Macromol.* **51**, 1498 (2018).
- [10] T. Rosén, B. S. Hsiao, and L. D. Söderberg, Elucidating the opportunities and challenges for nanocellulose spinning, *Adv. Mater.* **33**, 2001238 (2021).
- [11] D. Klemm, F. Kramer, S. Moritz, T. Lindström, M. Ankerfors, D. Gray, and A. Dorris, Nanocelluloses: a new family of nature-based materials, *Angew. Chem., Int. Ed.* **50**, 5438 (2011).
- [12] T. Li, C. Chen, A. H. Brozena, J. Zhu, L. Xu, C. Driemeier, J. Dai, O. J. Rojas, A. Isogai, L. Wågberg *et al.*, Developing fibrillated cellulose as a sustainable technological material, *Nature (London)* **590**, 47 (2021).
- [13] K. M. Håkansson, A. B. Fall, F. Lundell, S. Yu, C. Krywka, S. V. Roth, G. Santoro, M. Kvik, L. P. Wittberg, L. Wågberg *et al.*, Hydrodynamic alignment and assembly of nanofibrils resulting in strong cellulose filaments, *Nat. Commun.* **5**, 4018 (2014).
- [14] N. Mittal, F. Ansari, K. Gowda, V. C. Brouzet, P. Chen, P. T. Larsson, S. V. Roth, F. Lundell, L. Wågberg, N. A. Kotov *et al.*, Multiscale control of nanocellulose assembly: transferring remarkable nanoscale fibril mechanics to macroscale fibers, *ACS Nano* **12**, 6378 (2018).
- [15] A. Walther, J. V. Timonen, I. Díez, A. Laukkanen, and O. Ikkala, Multifunctional high-performance biofibers based on wet-extrusion of renewable native cellulose nanofibrils, *Adv. Mater.* **23**, 2924 (2011).
- [16] H. Voisin, L. Bergström, P. Liu, and A. P. Mathew, Nanocellulose-based materials for water purification, *Nanomater.* **7**, 57 (2017).
- [17] P. R. Sharma, S. K. Sharma, T. Lindström, and B. S. Hsiao, Water purification: Nanocellulose-enabled membranes for water purification: Perspectives (adv. sustainable syst. 5/2020), *Adv. Sust. Syst.* **4**, 2070009 (2020).
- [18] J. Rostami, K. Gordeyeva, T. Bensselfelt, E. Lahchaichi, S. A. Hall, A. V. Riazanova, P. A. Larsson, G. C. Ciftci, and L. Wågberg, Hierarchical build-up of bio-based nanofibrous materials with tunable metal-organic framework biofunctionality, *Mater. Today* **48**, 47 (2021).
- [19] W. Czaja, A. Krystynowicz, S. Bielecki, and R. M. Brown Jr, Microbial cellulose—the natural power to heal wounds, *Biomater.* **27**, 145 (2006).
- [20] R. J. Hickey and A. E. Pelling, Cellulose biomaterials for tissue engineering, *Front. Bioeng. Biotechnol.* **7**, 45 (2019).
- [21] M. Nordenström, T. Bensselfelt, R. Hollertz, S. Wennmalm, P. A. Larsson, A. Mehandzhyski, N. Rolland, I. Zozoulenko, D. Söderberg, and L. Wågberg, The structure of cellulose nanofibril networks at low concentrations and their stabilizing action on colloidal particles, *Carb. Poly.* **297**, 120046 (2022).
- [22] O. Eskilson, S. B. Lindström, B. Sepulveda, M. M. Shahjamali, P. Güell-Grau, P. Sivlér, M. Skog, C. Aronsson, E. M. Björk, N. Nyberg *et al.*, Self-assembly of mechanoplasmonic bacterial cellulose-metal nanoparticle composites, *Adv. Funct. Mater.* **30**, 2004766 (2020).
- [23] J. Yao, P. Ji, B. Wang, H. Wang, and S. Chen, Color-tunable luminescent macrofibers based on cdte qds-loaded bacterial cellulose nanofibers for ph and glucose sensing, *Sens. Act. B* **254**, 110 (2018).
- [24] M. M. Hamed, A. Hajian, A. B. Fall, K. Hakansson, M. Salajkova, F. Lundell, L. Wågberg, and L. A. Berglund, Highly conducting, strong nanocomposites based on nanocellulose-assisted aqueous dispersions of single-wall carbon nanotubes, *ACS Nano* **8**, 2467 (2014).
- [25] N. Amiralian, M. Mustapic, M. S. A. Hossain, C. Wang, M. Konarova, J. Tang, J. Na, A. Khan, and A. Rowan, Magnetic nanocellulose: A potential material for removal of dye from water, *J. Haz. Mater.* **394**, 122571 (2020).
- [26] C.-N. Wu, T. Saito, S. Fujisawa, H. Fukuzumi, and A. Isogai, Ultrastrong and high gas-barrier nanocellulose/clay-layered composites, *Biomacromol.* **13**, 1927 (2012).
- [27] A. Liu, A. Walther, O. Ikkala, L. Belova, and L. A. Berglund, Clay nanopaper with tough cellulose nanofiber matrix for fire retardancy and gas barrier functions, *Biomacromol.* **12**, 633 (2011).
- [28] B. W. An, S. Heo, S. Ji, F. Bien, and J.-U. Park, Transparent and flexible fingerprint sensor array with multiplexed detection of tactile pressure and skin temperature, *Nat. Commun.* **9**, 2458 (2018).
- [29] See Supplemental Material at <http://link.aps.org/supplemental/10.1103/PhysRevE.108.014607> for further details of sample preparation, experiments, and simulations, which includes Refs. [38–47].
- [30] A. Ogston, The spaces in a uniform random suspension of fibres, *Trans. Faraday Soc.* **54**, 1754 (1958).
- [31] R. Wang, T. Rosen, C. Zhan, S. Chodankar, J. Chen, P. R. Sharma, S. K. Sharma, T. Liu, and B. S. Hsiao, Morphology and flow behavior of cellulose nanofibers dispersed in glycols, *Macromol.* **52**, 5499 (2019).
- [32] MATLAB documentation: Coefficient of determination (r-squared), <https://www.mathworks.com/help/stats/coefficient-of-determination-r-squared.html>, accessed: 2023-06-14.
- [33] V. Pryamitsyn and V. Ganesan, Dynamics of Probe Diffusion in Rod Solutions, *Phys. Rev. Lett.* **100**, 128302 (2008).
- [34] V. Pryamitsyn and V. Ganesan, Screening of hydrodynamic interactions in brownian rod suspensions, *J. Chem. Phys.* **128**, 134901 (2008).
- [35] M. M. Tirado, C. L. Martínez, and J. G. de la Torre, Comparison of theories for the translational and rotational diffusion coefficients of rod-like macromolecules. Application to short DNA fragments, *J. Chem. Phys.* **81**, 2047 (1984).
- [36] M. Ernst, T. John, M. Guenther, C. Wagner, U. F. Schaefer, and C.-M. Lehr, A model for the transient subdiffusive behavior of particles in mucus, *Biophys. J.* **112**, 172 (2017).

- [37] Z. Xu, X. Dai, X. Bu, Y. Yang, X. Zhang, X. Man, X. Zhang, M. Doi, and L.-T. Yan, Enhanced heterogeneous diffusion of nanoparticles in semiflexible networks, *ACS Nano* **15**, 4608 (2021).
- [38] T. Saito, S. Kimura, Y. Nishiyama, and A. Isogai, Cellulose nanofibers prepared by tempo-mediated oxidation of native cellulose, *Biomacromol.* **8**, 2485 (2007).
- [39] S. Katz, R. P. Beatson *et al.*, The determination of strong and weak acidic groups in sulfite pulps, *Svensk papperstidning* **87**, 48 (1984).
- [40] T. Rosén, R. Wang, H. He, C. Zhan, S. Chodankar, and B. S. Hsiao, Understanding ion-induced assembly of cellulose nanofibrillar gels through shear-free mixing and in situ scanning-saxs, *Nanoscale Adv.* **3**, 4940 (2021).
- [41] T. Rosén, R. Wang, H. He, C. Zhan, S. Chodankar, and B. S. Hsiao, Shear-free mixing to achieve accurate temporospatial nanoscale kinetics through scanning-saxs: Ion-induced phase transition of dispersed cellulose nanocrystals, *Lab Chip* **21**, 1084 (2021).
- [42] L. Geng, X. Peng, C. Zhan, A. Naderi, P. R. Sharma, Y. Mao, and B. S. Hsiao, Structure characterization of cellulose nanofiber hydrogel as functions of concentration and ionic strength, *Cellulose* **24**, 5417 (2017).
- [43] D. I. Sagdeev, M. G. Fomina, and I. M. Abdulagatov, Density and viscosity of propylene glycol at high temperatures and high pressures, *Fluid Phase Equilib.* **450**, 99 (2017).
- [44] A. P. Chatterjee, A simple model for the pore size distribution in random fibre networks, *J. Phys.: Condens. Matter* **24**, 375106 (2012).
- [45] D. Lumma, L. Lurio, S. Mochrie, and M. Sutton, Area detector based photon correlation in the regime of short data batches: Data reduction for dynamic x-ray scattering, *Rev. Sci. Instrum.* **71**, 3274 (2000).
- [46] Sasview 5.0.4 documentation: Polydispersity and orientational distributions, <https://www.sasview.org/docs/user/qtgui/Perspectives/Fitting/pd/polydispersity.html>, accessed: 2022-04-14.
- [47] L. Feigin, D. I. Svergun *et al.*, *Structure Analysis by Small-Angle X-Ray and Neutron Scattering*, Vol. 1 (Springer, Berlin, 1987).